Highly efficient electrocatalysis of oxygen to hydroxyl radical by FeN$_2$O$_2$ single-atom catalyst for refractory organic pollutant removal

Zijun Tan [a], Peike Cao [a], Shuo Chen [a], Hongtao Yu [a], Yan Su [b], Xie Quan [a],[*]

[a] *Key Laboratory of Industrial Ecology and Environmental Engineering (Ministry of Education, China), School of Environmental Science and Technology, Dalian University of Technology, Dalian 116024, China*
[b] *Key Laboratory of Materials Modification by Laser, Ion and Electron Beams (Ministry of Education), School of Physics, Dalian University of Technology, Dalian 116024, China*

ARTICLE INFO

ABSTRACT

The heterogeneous electro-Fenton (Hetero-EF) provides an effective and environmentally friendly method for refractory pollutants removal by strongly oxidative •OH. However, the •OH generation shows an insufficient activity in activating H$_2$O$_2$ to •OH due to the too strong H$_2$O$_2$ binding on the catalytic site. Here, an iron single-atom FeN$_2$O$_2$ catalyst anchored on hollow spherical porous carbon (FeN$_2$O$_2$-HPC) was designed to enhance •OH production by modulating the H$_2$O$_2$ binding. The FeN$_2$O$_2$-HPC Hetero-EF system showed a •OH production rate of 25.0 µmol h^{-1} and kinetic rate constant of 2.06 h^{-1} for phenol removal, which exceeded the FeN$_4$ catalyst (the most reported iron single-atom). Density function theory calculations revealed that FeN$_2$O$_2$ could lower the H$_2$O$_2$ adsorption energy and energy barrier of H$_2$O$_2$ activation to •OH compared with FeN$_4$, thus enhancing •OH production. This work gives a new insight into the •OH generation enhancement of Hetero-EF by modulating single-atom coordination environment for refractory pollutants removal.

1. Introduction

The refractory organic wastewater effluent after the conventional biological treatment generally cannot meet the discharge standard due to the presence of highly-concentrated toxic and non-biodegradable organic pollutants. Advanced oxidation processes (AOPs) are the effective technologies to degrade the refractory organic pollutants via the generation of oxidative radicals, presenting the favorable practices for the advanced treatment of the coking wastewaters [1,2]. Fenton technology shows multiple advantages of high production rate of •OH, high oxidizing ability and high removal and mineralization efficiency for refractory organic pollutants [3–5]. The strongly oxidative •OH can be produced via the decomposition of H$_2$O$_2$ catalyzed by active Fe^{2+} in an acidic solution. Unfortunately, the Fenton technology suffers from the knotty issues of narrow operation pH range (pH 3–4), high expense of Fenton agents (iron salts and H$_2$O$_2$) and the production of iron sludge. Moreover, the storage and transportation of highly-concentrated H$_2$O$_2$ (30 wt%) poses an explosion risk.

The heterogeneous electro-Fenton (Hetero-EF) technology can produce •OH in situ via the two-step combination of H$_2$O$_2$ generation and H$_2$O$_2$ activation using a solid iron-based cathode. The Hetero-EF shows the benefits of removing the dependence on the H$_2$O$_2$ agent, no iron sludge generation and broadening the pH range of 3–10 [6,7]. The Hetero-EF process involves the two key steps: the in-situ production of H$_2$O$_2$ via a two-electron oxygen reduction reaction (ORR), and the catalytic decomposition of H$_2$O$_2$ for the generation of •OH [8,9]. In order to achieve a higher •OH production rate, it is crucial to design a bifunctional catalyst for selective H$_2$O$_2$ synthesis and activation of H$_2$O$_2$ for generating •OH. Previous studies suggested that the activity and selectivity of H$_2$O$_2$ production via two-electron ORR were highly related with the binding energy of the *OOH intermediate on a catalyst [10,11]. Oxygen-doped carbon materials were reported to be 2e$^-$ ORR selective for producing H$_2$O$_2$, due to the weak binding with the *OOH intermediate and the facile preservation of O-O bond [12–14]. Another key step of the Hetero-EF process is the activation of H$_2$O$_2$ for producing •OH. Many Fe-based materials were reported to be active to activate H$_2$O$_2$ to •OH, whereas these catalysts showed the disadvantages of low atom utilization efficiency, low activity and poor durability due to the agglomeration of metal irons [15–17].

Single-atom catalysts (SACs) featured with highly dispersed metal atomic sites anchored on a support material exhibit high atom utilization efficiency that can enhance the catalytic activity significantly

---

* Corresponding author.
  E-mail address: quanxie@dlut.edu.cn (X. Quan).

[18–20]. Significant efforts have been devoted to developing efficient Fe-based SACs (Fe–N–C) with high stability and highly-efficient generation of •OH in Hetero-EF process for the removal of refractory organic pollutants [21–23]. However, the Fe-based SACs catalysts with a FeN_4 configuration have been reported to be more selective for the electro-reduction of O_2 and H_2O_2 to produce H_2O rather •OH, due to their strong binding with these adsorbates [24–26]. The performance of activating H_2O_2 for the generation of •OH can be enhanced by lowering the binding energy of H_2O_2 on the FeN_4 catalysts in principle. Many studies suggested that the adsorption of electrocatalytic reaction intermediates on the catalysts could be tuned by modulating the electronic property of the active sites [27–30]. With the introduction of O atoms, the adsorption of reaction intermediates on Fe-N_4 SACs catalysts can be weakened by O-doping coordination configuration [31]. We can anticipate that the adsorption energy of H_2O_2 on the FeN_4 catalyst can be reduced by partially replacing the N coordination atom with O with a higher electronegativity, thus promoting the production of •OH [32].

In this work, we prepared an iron single-atom catalyst with the FeN_2O_2 coordination anchored on a hollow spherical porous carbon (FeN_2O_2-HPC) acted as the Hetero-EF catalyst for enhancing •OH production. The oxygen-doped hollow spherical porous carbon could catalyze the production of H_2O_2 and FeN_2O_2 site could boost the generation of •OH via the activation of the as-generated H_2O_2. Experimental results showed that the FeN_2O_2-HPC catalyst exhibited a higher •OH production rate (25.0 μmol h^{-1}) than that of the FeN_4-HPC (8.3 μmol h^{-1}). Density functional theory (DFT) calculations revealed that the introduction of O atoms in coordination environment on FeN_2O_2-HPC could reduce the binding energies of *H_2O_2 and energy barrier of H_2O_2 activation to •OH compared with the Fe-N_4 site, thereby facilitating more efficient •OH production and organic contaminants removal.

2. Materials and methods

2.1. Synthesis of iron single-atom anchored on a hollow spherical porous carbon (Fe-HPC)

The FeN_2O_2-HPC catalysts were synthesized via SiO_2 as a hard template process followed by an annealing method. Briefly, 10 mL ultrapure water, 70 mL ethanol and 3 mL ammonia (25 wt%) were mixed into the solution. After 10 min, 3.5 mL tetraethyl orthosilicate (TEOS) was added into the solution mixture with stirring at room temperature. After 20 min, 3.5 mmol of resorcinol, 0.6 mL of formaldehyde and a certain amount of $FeCl_3$ solution were added to the solution above and stirred for 24 h. The obtained precipitate was rinsed several times with ethanol and ultrapure water, and dried at 60 °C. Afterwards, the powder was annealed at 700 °C (ramping rate of 5 °C min^{-1}) for 5 h in N_2 atmosphere. Consequently, in order to remove SiO_2 impurities, the obtained powder was soaked in NaOH solution (2 mol L^{-1}) for 24 h, washed several times and followed by desiccated at 60 °C. The obtained product was denoted as FeN_2O_2-HPC. For comparison, the samples with different amounts of Fe loading and without Fe were prepared (denoted as Fe_x-HPC, x represents the mass of Fe loading on HPC). The iron single-atom catalyst with the FeN_4 coordination anchored on a hollow spherical porous carbon (FeN_4-HPC) was prepared as follows. 30 mg HPC and 10 mg $FeCl_3$ were added into N, N-dimethylformamide (DMF) (60 mL). After 2 h ultrasound treatment, the solution was heated at 80 °C to dry the solution above. Then, the as-obtained powder was treated at 700 °C for 2 h under a nitrogen atmosphere. Eventually, the as-obtained powder was washed with 1 mol L^{-1} HCl at 80 °C for 12 h and dried at 60 °C under vacuum for 24 h.

2.2. Electrochemical measurements

The electrochemical experiments of •OH production and pollutant removal by the Hetero-EF process were performed in a single-compartment reactor with a three-electrode system. The working electrode was prepared in the following procedure: 5 mg of obtained catalyst was added into 1.9 mL ultrapure water and 0.1 mL Nafion (5 wt %) solution. After ultrasonicated for 2 hours, the catalyst ink was coated onto carbon cloth (HCP330N), with effective working area of 12 cm^2. Pt sheet, and saturated calomel electrode (SCE) were used as the counter electrode and reference electrode, respectively. The potential versus SCE was converted to a potential versus the reversible hydrogen electrode (RHE) by calculation with the assistance of the Nernst equation (E_{RHE} = E_{SCE} + 0.059 × pH + 0.2415). The degradation experiment was performed in 30 mL of 0.05 mol L^{-1} Na_2SO_4 electrolyte containing 20 mg L^{-1} organic pollutants at an applied potential of −0.4 V vs. SCE, with continuous O_2 aerating at a flow rate of 30 mL min^{-1}. The concentration of generated •OH was measured via probe reaction of salicylic acid (SA) and •OH, with 2,3-dihydroxybenzoic acid (2,3-DHBA), and 2,5-dihydroxibenzoic acid (2,5-DHBA) acting as probes and measured by using high performance liquid chromatography (HPLC) [33,34]. The initial pH was adjusted by using H_2SO_4 (0.2 mol L^{-1}) and NaOH (0.2 mol L^{-1}). The treatment of the secondary effluent of actual coking wastewater is performed to evaluate the performance of the Hetero-EF of FeN_2O_2-HPC. The chemical oxygen demand (COD) and total organic carbon (TOC) removal of secondary effluent of actual coking wastewater was measured.

(More experimental methods and details were provided in Supporting Information.)

3. Results and discussion

3.1. Iron single-atom catalysts characterization

The morphology and structure of all iron single-atom anchored on a hollow spherical porous carbon (Fe-HPC) catalysts were observed by the scanning electron microscopy (SEM) and transmission electron microscopy (TEM). As depicted in Fig. 1a-b and S1, all Fe-HPC catalysts showed a spherical morphology with a diameter of 400 nm. As observed from the TEM images in Fig. 1c, the hollow spherical architecture was formed with a thickness of 25 nm and no iron particles were observed. The elemental mapping from energy dispersive spectrum (Figure S2) revealed the uniform distribution of Fe, C, O and N elements, suggesting that the Fe species were atomically dispersed on the oxygen-doped carbon. The crystal structures of the obtained Fe-HPCs were measured by X-ray diffraction (XRD). All Fe-HPCs catalysts exhibited one diffraction peaks at 23°, which was corresponding to the typical peaks of (002) of graphitic carbon plane (Figure S3), confirming that no iron-related crystal phases were detected [35]. Furthermore, the aberration-corrected high-angle annular dark-field scanning transmission electron microscopy (AC-HAADF-STEM) image in Fig. 1d revealed that atomic-scaled bright dots were well distributed on the hollow carbon sphere and no visible nanoparticles or sub-nanometer clusters were observed, further confirming the existence of Fe single atoms. The element mapping image in Figs. 1e-1f displayed that Fe, C, O and N atoms were uniformly dispersed on hollow carbon spheres, which is consistent with the results of TEM images. The Fe_x-HPC catalysts with different loadings of iron were prepared as a comparison. The iron loadings of the Fe_x-HPC catalysts measured by inductively coupled plasma optical emission spectrometry (ICP-OES) were determined to be 0.25, 0.47, 1.05, 1.52 and 7.1 wt% on $Fe_{0.25}$-HPC, FeN_2O_2-HPC, $Fe_{1.05}$-HPC, $Fe_{1.52}$-HPC and $Fe_{7.1}$-HPC, respectively. (Table S2). As Figure S4 depicted, the diffraction peaks assigned to the Fe nanocrystals were observed from the XRD spectra of the $Fe_{7.1}$-HPC due to the high loading of Fe. The FeN_4-HPC catalyst was prepared to demonstrate the role of the coordination environment of iron single-atom. The Fe loadings were 0.47 and 0.45 wt% for the FeN_2O_2-HPC and FeN_4-HPC catalysts, respectively.

The chemical compositions of the Fe-HPCs catalysts were measured by X-ray photoelectron spectroscopy (XPS). As displayed in Figure S5, all catalysts showed the characteristic XPS signals of C, N, and O
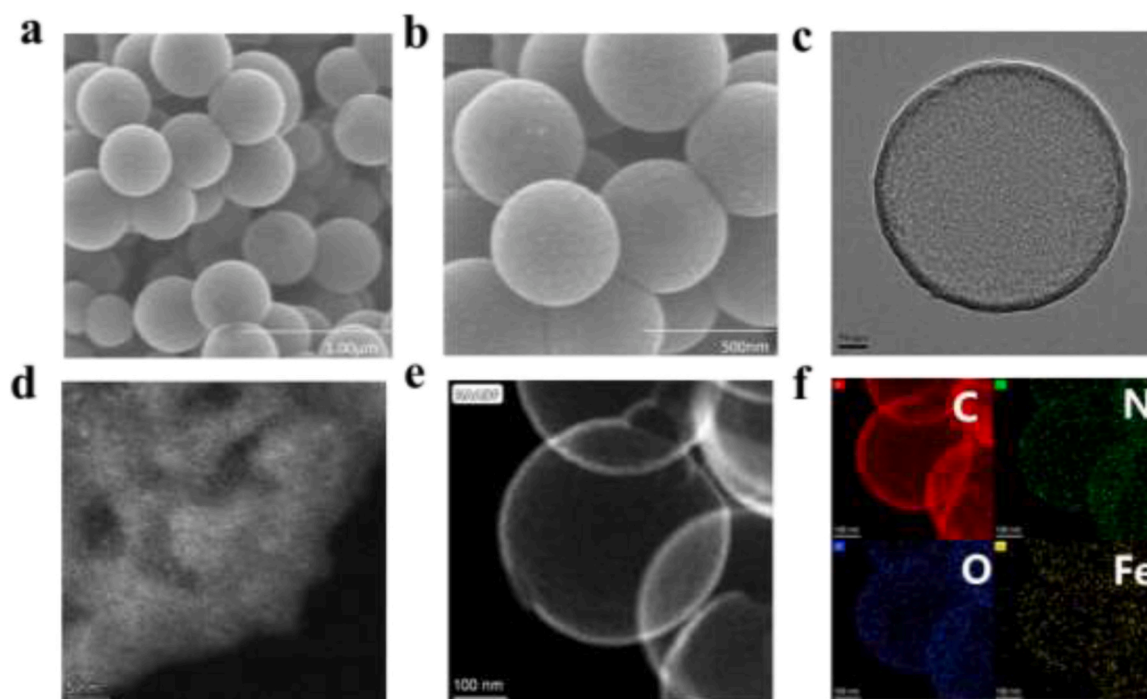
Fig. 1. (a, b) SEM image and (c) TEM image of the FeN$_2$O$_2$-HPC, (d) AC-HAADF-STEM image and (e, f) Elemental mapping images of the FeN$_2$O$_2$-HPC.

elements (Table S3). As exhibited in Figure S6, the high-resolution XPS spectra of Fe showed weak signals in FeN$_2$O$_2$-HPC and FeN$_4$-HPC due to the low iron loadings. To reveal the coordination structure of the FeN$_2$O$_2$-HPC, the X-ray absorption near-edge spectroscopy (XANES) of the Fe K-edge was analyzed. As displayed in Fig. 2a, the near-edge absorption energy of FeN$_2$O$_2$-HPC was located between that of the ferrous oxide (FeO) and ferric oxide (Fe$_2$O$_3$) reference samples, indicating that the oxidation state of iron atoms should be $+2 \sim +3$ [26]. The
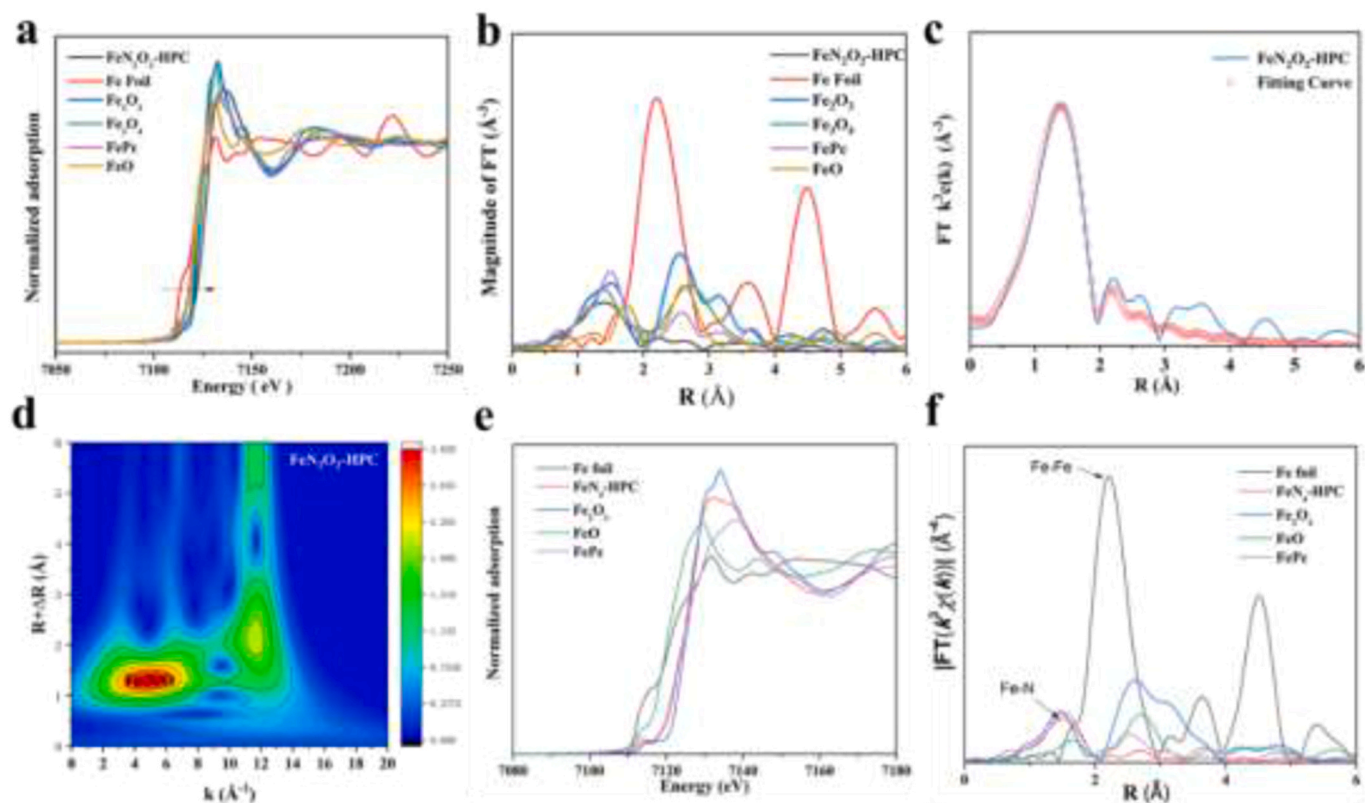

Fig. 2. (a, b) XANES spectra, FT-EXAFS spectra at R space of Fe K-edge, (c) EXAFS fitting curves and (d) the WT contour plot for FeN$_2$O$_2$-HPC; (e, f) XANES spectra, FT-EXAFS spectra at R space of Fe K-edge for FeN$_4$-HPC.

k^3-weighted $\chi(k)$ function Fourier-transformed extended X-ray absorption fine structure (FT-EXAFS) of the Fe K-edge of FeN_2O_2-HPC showed a main peak centered at around 1.4 Å that could be assigned to the Fe−N/O coordination (Fig. 2b) [32]. The coordination configuration for the FeN_2O_2-HPC was analyzed by a least-squares fitting of the FT-EXAFS. The fitting curves displayed in Fig. 2c and Figure S7 showed that the coordination number of Fe atoms in FeN_2O_2-HPC was about 4. As depicted in Table S4, the bond length of the Fe atom and the coordination atoms of N or O were 1.98 and 1.82 Å, respectively, suggesting that the atomically dispersed Fe were coordinated by two N and two O atoms as indicated by the FeN_2O_2 configuration. As shown in Fig. 2d, the wavelet transformed extended X-ray absorption fine structure (WT-EXAFS) of FeN_2O_2-HPC exhibited one obvious value at the coordinate of (4.8 Å^{-1}, 1.4 Å) that were corresponding to the Fe–N/O bonding, demonstrating the N, O dual coordination of Fe atoms. Notably, comparing with WT-EXAFS of standard samples such as Fe foil (Figure S8), no obvious peak of Fe−Fe coordination with the maximum region located at (8.2 Å^{-1}, 2.2 Å) were observed in the FeN_2O_2-HPC, suggesting the isolated dispersion of single-atom Fe. As a comparison, the configuration of the FeN_4-HPC was analyzed. The near-edge absorption edge (Fig. 2e), the FT-EXAFS and EXAFS fitting curves of Fe atoms in the FeN_4-HPC clearly revealed the dominant Fe−N_4 structure [26]. Significantly, no Fe−Fe bond was found in FeN_4-HPC, verifying the Fe single-atom centers coordinated with N species (Fig. 2f and S9–10, Table S5). Based on the results above, the coordination structure of the atomically dispersed Fe of the FeN_2O_2-HPC was proposed to be Fe−N_2O_2, as indicated by density functional theory (DFT) calculations.

3.2. Electrochemical performance by Fe-HPCs

The electrocatalytic property of the Fe-HPCs for ORR activity was investigated by linear scan voltammetry (LSV) measurements. As depicted in Figure S11, all Fe-HPCs catalysts exhibited a noticeable characteristic peak in O_2-saturated electrolyte compared with Ar-saturated electrolyte, suggesting that Fe-HPCs exhibited electrocatalytic ORR activity. The electrocatalytic two-electron ORR activity and selectivity for the Fe-HPCs were evaluated through using a rotating ring-disk electrode (RRDE). As shown in Figure S12, the polarization curves collected on the disk and Pt ring electrodes represented the O_2 reduction and H_2O_2 oxidation, respectively. The HPC exhibited ~87 % of H_2O_2 selectivity at –0.35–0.35 V vs. RHE, suggesting that HPC showed higher two-electron ORR selectivity to H_2O_2 production. The H_2O_2 production rate (kp, H_2O_2) of the HPC was measured to be 316.7 µmol h^{-1} (Figs. 3a and S13). Notably, the FeN_2O_2-HPC and FeN_4-HPC showed lower production rates (61.9 and 51.7 µmol h^{-1}) than HPC, suggesting the as-generated H_2O_2 can be decomposed by the loaded Fe sites. The *in-situ* Fourier transform infrared (FT-IR) spectroscopy was employed to demonstrate the existence of intermediates in the conversion from oxygen to hydrogen peroxide. The *in-situ* FT-IR spectra was recorded by varying the applied potential from 0 to 0.4 V vs. RHE in O_2-saturated 0.05 mol L^{-1} Na_2SO_4 solution (pH 7), and the *in-situ* FT-IR spectrum (the gray curve) without the applied potential was also recorded as the control. As shown in Figure S14, the band at around 1419 cm^{-1} was attributed to the O−O stretching mode of adsorbed O_2 molecules on the FeN_2O_2-HPC surface, which was the prerequisite for ORR [36]. Notably, a main band at ~1224 cm^{-1} and a weak band at

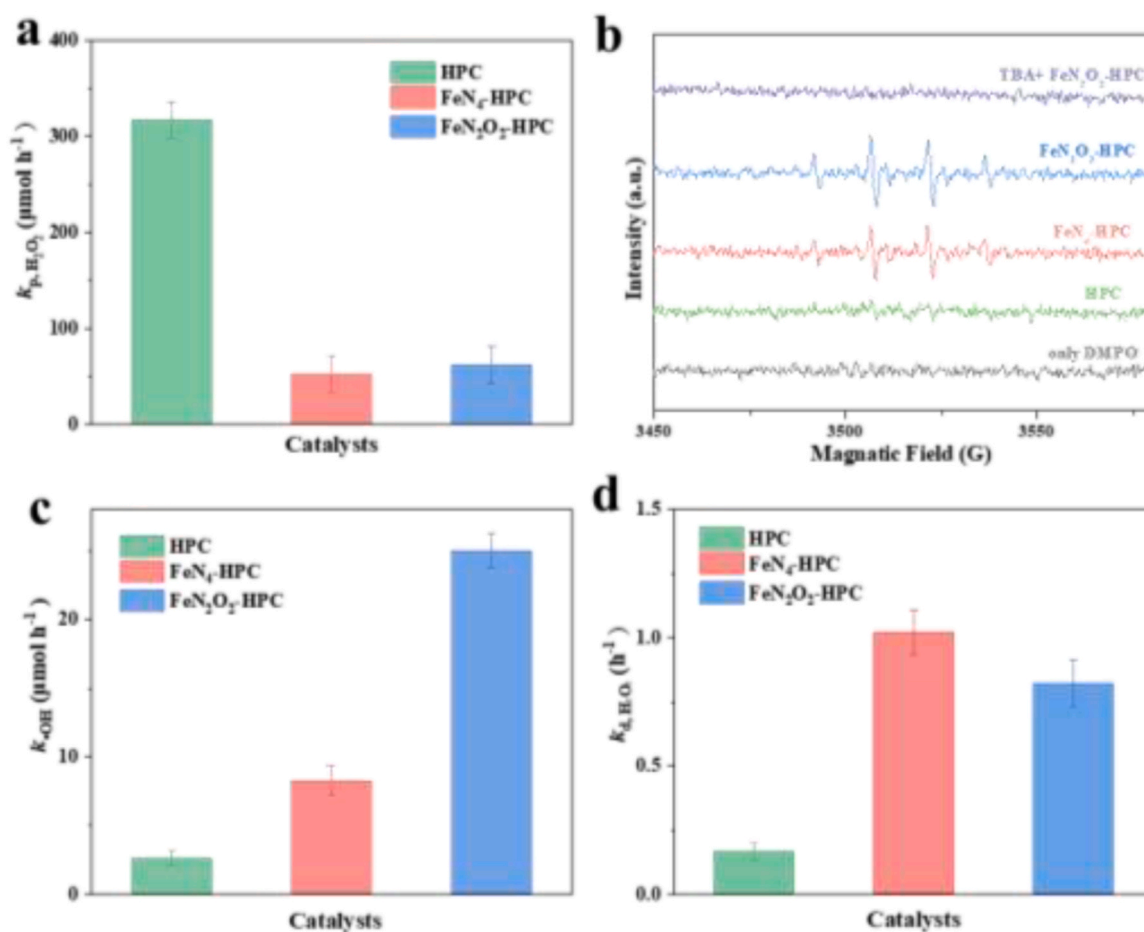**Fig. 3.** (a) k_{p}, H_2O_2 of the HPC, FeN_4-HPC, and FeN_2O_2-HPC from ORR; (b) EPR spectrum obtained by the Hetero-EF system of the FeN_2O_2-HPC, FeN_4-HPC, HPC, FeN_2O_2-HPC and with TBA addition; (c) $k_{\bullet OH}$ produced in Hetero-EF system of the HPC, FeN_4-HPC, and FeN_2O_2-HPC (d) $k_{d,}$ H_2O_2 from the activation of H_2O_2 in Ar-saturated electrolyte. Conditions: pH = 7, potential = –0.4 V vs. SCE, O_2 flow rate = Ar flow rate = 30 mL min^{-1}.

~1390 cm^{-1} appeared and increased with the negative shifting potential for FeN$_2$O$_2$-HPC. These were assigned to the O−O stretching mode of surface-adsorbed *OOH and the OOH bending mode of surface-adsorbed *H$_2$O$_2$, respectively [37,38]. The results of *in-situ* FT-IR confirm the presence of *OOH and *H$_2$O$_2$ intermediates during •OH generation.

Furthermore, the electroreduction of H$_2$O$_2$ towards •OH was first investigated through the extra addition of H$_2$O$_2$ in Ar-saturated electrolyte. As depicted in Figure S15, after adding 3 mM of H$_2$O$_2$, all catalysts exhibited obvious currents of the reduction reaction. Both FeN$_2$O$_2$-HPC and FeN$_4$-HPC exhibited higher current densities of H$_2$O$_2$ reduction than the HPC, demonstrating the important role of Fe single-atom sites in reducing H$_2$O$_2$. The •OH production was measured qualitatively on an electron paramagnetic resonance (EPR) spectrometer with 5,5-dimethyl-1- pyrroline N-oxide (DMPO) as •OH trapping agent. As displayed in Fig. 3b, no noticeable signal was detected by sole DMPO. The FeN$_2$O$_2$-HPC Hetero-EF system showed typical quartet characteristic signals that could be assigned to the DMPO-•OH adduct, and the intensity of signals obviously decreased after adding tert-butyl alcohol (TBA) as the •OH scavenger, revealing the •OH production by the FeN$_2$O$_2$-HPC Hetero-EF system. Notably, FeN$_2$O$_2$-HPC exhibited the highest intensity of signal than that of FeN$_4$-HPC and HPC catalysts, indicating the favorable •OH production ability on FeN$_2$O$_2$-HPC. We quantitatively measured the •OH yield (method in the Supporting Information). As exhibited in Figure S16 and Fig. 3c, the FeN$_2$O$_2$-HPC Hetero-EF system delivered a continuous increase in accumulated •OH concentration with the extension of reaction time. The •OH production rate (k$_{•OH}$) on the FeN$_2$O$_2$-HPC achieved 25.0 μmol h^{-1}, which was higher than that of FeN$_4$-HPC (8.3 μmol h^{-1}) and HPC (2.6 μmol h^{-1}), and exceeded that of the state-of-the-art advanced oxidation processed reported catalysts (Table S6) [21,22,33,39,40]. The FeN$_2$O$_2$-HPC catalyst delivered 3 times higher yield of •OH than the FeN$_4$-HPC, suggesting the crucial role of the FeN$_2$O$_2$ coordination for enhancing the activation of H$_2$O$_2$ to •OH. Moreover, the activity in activating H$_2$O$_2$ for •OH generation was investigated by electrocatalytic H$_2$O$_2$ reduction, where 1 mmol L^{-1} H$_2$O$_2$ was added into oxygen-free 0.05 mol L^{-1} Na$_2$SO$_4$ electrolyte. As shown in Figure S17, the amount of H$_2$O$_2$ significantly decreased on FeN$_2$O$_2$-HPC and FeN$_4$-HPC while a slight downward trend of H$_2$O$_2$ concentration was observed on HPC catalyst. The H$_2$O$_2$ decomposition rate of the catalyst (k$_{d,}$ H$_2$O$_2$) were measured (Fig. 3d), and FeN$_2$O$_2$-HPC and FeN$_4$-HPC exhibited faster k$_{d,}$ H$_2$O$_2$ of 0.82 h^{-1} and 1.02 h^{-1} than HPC (0.17 h^{-1}), confirming the crucial role of the FeN$_2$O$_2$ sites for enhancing the activation of H$_2$O$_2$ to •OH. Based on the above experiment results, it could be concluded that the high •OH production on Fe-HPC SACs involved two steps, where H$_2$O$_2$ was selectively produced on oxygen-doped carbon matrix and subsequently the as-generated H$_2$O$_2$ was activated to •OH by active Fe single-atom sites.

Furthermore, the impact of Fe loadings of Fe$_x$-HPCs (x = 0.25, 1.05, 1.52 and 7.1, x represents the loadings of Fe) on the •OH generation was investigated. As Figure S18 displayed, the H$_2$O$_2$ generation of the Fe$_x$-HPCs catalysts were measured to be 61.9 – 156.8 μmol h^{-1}, which were lowered than the HPC, suggesting iron sites could decompose the as-generated H$_2$O$_2$. The •OH production rate of the Fe$_x$-HPCs catalysts followed the trend of HPC (25.9 mmol L^{-1} g$_{cat}^{-1}$) < Fe$_{7.1}$-HPC (66.8 mmol L^{-1} g$_{cat}^{-1}$) < Fe$_{0.25}$-HPC (87.9 mmol L^{-1} g$_{cat}^{-1}$) < Fe$_{1.52}$-HPC (109.5 mmol L^{-1} g$_{cat}^{-1}$) < Fe$_{1.05}$-HPC (155.4 mmol L^{-1} g$_{cat}^{-1}$) < FeN$_2$O$_2$-HPC (249.7 mmol L^{-1} g$_{cat}^{-1}$), suggesting that the FeN$_2$O$_2$-HPC had the optimal Fe loading for •OH generation. Compared with FeN$_2$O$_2$-HPC with an iron loading of 0.47 wt%, the decreased •OH yield on Fe$_{1.05}$-NPC, Fe$_{1.52}$-NPC and Fe$_{7.1}$-NPC could be attributed to the metal agglomeration due to the excess loading of Fe, resulting in the decreased number of the active sites for H$_2$O$_2$ activation to •OH.

3.3. Mechanism of O$_2$-to-•OH on the FeN$_2$O$_2$-HPC

To reveal the mechanism of •OH generation on the FeN$_2$O$_2$-HPC,

density function theory (DFT) calculations were performed. According to the EXAFS results in Fig. 2, two models of Fe-N$_2$O$_2$ (FeN$_2$O$_2$-HPC) and Fe-N4 (FeN$_4$-HPC) were constructed and optimized as shown in Figure S19a-b. We used the H$_2$O$_2$ adsorption on active sites as a description for the activity in •OH generation. As shown in Figure S20a-b and Table S7, the H$_2$O$_2$ adsorption energies of Fe-N$_2$O$_2$ and Fe-N$_4$ were –0.16 and –0.37 eV, respectively, demonstrating that the adsorption of H$_2$O$_2$ could be weakened by the Fe-N$_2$O$_2$ than the Fe-N$_4$. Fig. 4a-b showed the differential charge densities of the Fe-N$_2$O$_2$ and Fe-N$_4$. The charge state of the iron atom of Fe-N$_2$O$_2$ (1.00 |e|) was more positive than Fe-N$_4$ (1.08 |e|), suggesting that the charge state of Fe center atom could be modulated by the replacement of N of the coordination atoms with O. To explore the reason of the lower charge state of iron atom on Fe-N$_2$O$_2$ compared to Fe-N$_4$, the electronic work function of Fe-N$_2$O$_2$ and Fe-N$_4$ models were calculated. Generally, the electrons are more likely to migrate towards the sites with a higher electronic work function, and thus the sites own good ability to accept electrons, suggesting the higher charge state. As shown in Figure S21, Fe-N$_4$ exhibited higher electronic work function of 4.73 eV than that of Fe-N$_2$O$_2$ (4.35 eV), indicating a favorable electron-accepting ability. Thus the Fe-N$_2$O$_2$ (1.00 |e|) iron atom has a lower charge state compared to Fe-N$_4$ (1.08 |e|) and Fe-N$_4$ may be more easily to react with more electrons for two-electron H$_2$O$_2$ activation to H$_2$O rather than •OH. Furthermore, to clarify the changes in the Fe atomic valence electron layer during this process, the d-band center of Fe-N$_2$O$_2$ and Fe-N$_4$ models were also calculated. As shown in Fig. 4c-d, the d-band center (ε$_d$) of Fe-N$_2$O$_2$ (ε$_d$ = −1.20 eV) was lower than that of Fe-N$_4$ (ε$_d$ = −1.09 eV). Previous studies reported that the adsorption ability of catalysts between the active sites and the reaction species was dependent on the ε$_d$ of catalysts, where the lower adsorption of catalysts always accompanied with a lower position of ε$_d$ [41–43]. Thus, the enhanced catalytic activity of H$_2$O$_2$ to •OH on Fe-N$_2$O$_2$ could be attributed to the downward shift of the ε$_d$ of iron atoms. This result was also consistent with the calculated adsorption energy of H$_2$O$_2$ on Fe-N$_2$O$_2$ models. Fe-N$_2$O$_2$ showed a low electron density of Fe sites compared with Fe-N$_4$, manifesting the relative favorable one-electron reduction pathway of H$_2$O$_2$ for •OH. The weaken adsorption of H$_2$O$_2$ and effective electron transfer are beneficial for H$_2$O$_2$ reduction to •OH on Fe-N$_2$O$_2$, thus mitigating the issues of too strong binding of *H$_2$O$_2$ on the Fe sites to disproportionation to produce H$_2$O.

Furthermore, the production of radicals on two models was estimated via comparing the reaction free energies and kinetic barrier of forming •OH from *H$_2$O$_2$. The thermodynamic equations used in the free energy calculations were provided in Supporting Information. Generally, the negative free energy demonstrates that the reaction is thermodynamically favorable. As shown in Fig. 4e-f and Table S8, the free energies of forming •OH on the Fe-N$_2$O$_2$ site were –0.51 eV at electrode potential of 0.25 V vs. RHE, which was lower than that of the Fe-N$_4$ site of –0.32 eV, verifying that the •OH production on the Fe-N$_2$O$_2$ site was more favorable than Fe-N$_4$ site. The reaction kinetics were further presented in Fig. 4g-h. The step of adsorption of H$_2$O$_2$ to transition state (TS) formation is uphill on all calculated active sites, then the *OH desorption to forming •OH radicals was a downhill process of exothermal reaction. In the cases of Fe-N$_2$O$_2$, the rate determined step was the adsorption of H$_2$O$_2$, with a kinetic energy barrier of 0.11 eV, which was lower than that of Fe-N$_4$ site (0.23 eV). The •OH generation from *OH desorption on Fe-N$_2$O$_2$ site showed a lower exothermal energy of –0.76 eV than single Fe-N$_4$ site (–0.57 eV), implying that the Fe-N$_2$O$_2$ site was more thermodynamically favorable for H$_2$O$_2$ reduction to •OH. Obviously, a moderate *H$_2$O$_2$ adsorption is favorable to selectively catalyze •OH generation, whereas strong binding energy would result in a large energy barrier of H$_2$O$_2$ adsorption to TS formation on Fe-N$_4$ sites, causing production of H$_2$O.

Based on the results above, we proposed the mechanism of •OH generation on the FeN$_2$O$_2$-HPC catalysts in Fig. 5: O$_2$ is firstly adsorbed on the surface of the HPC for two-electron ORR pathway to produce
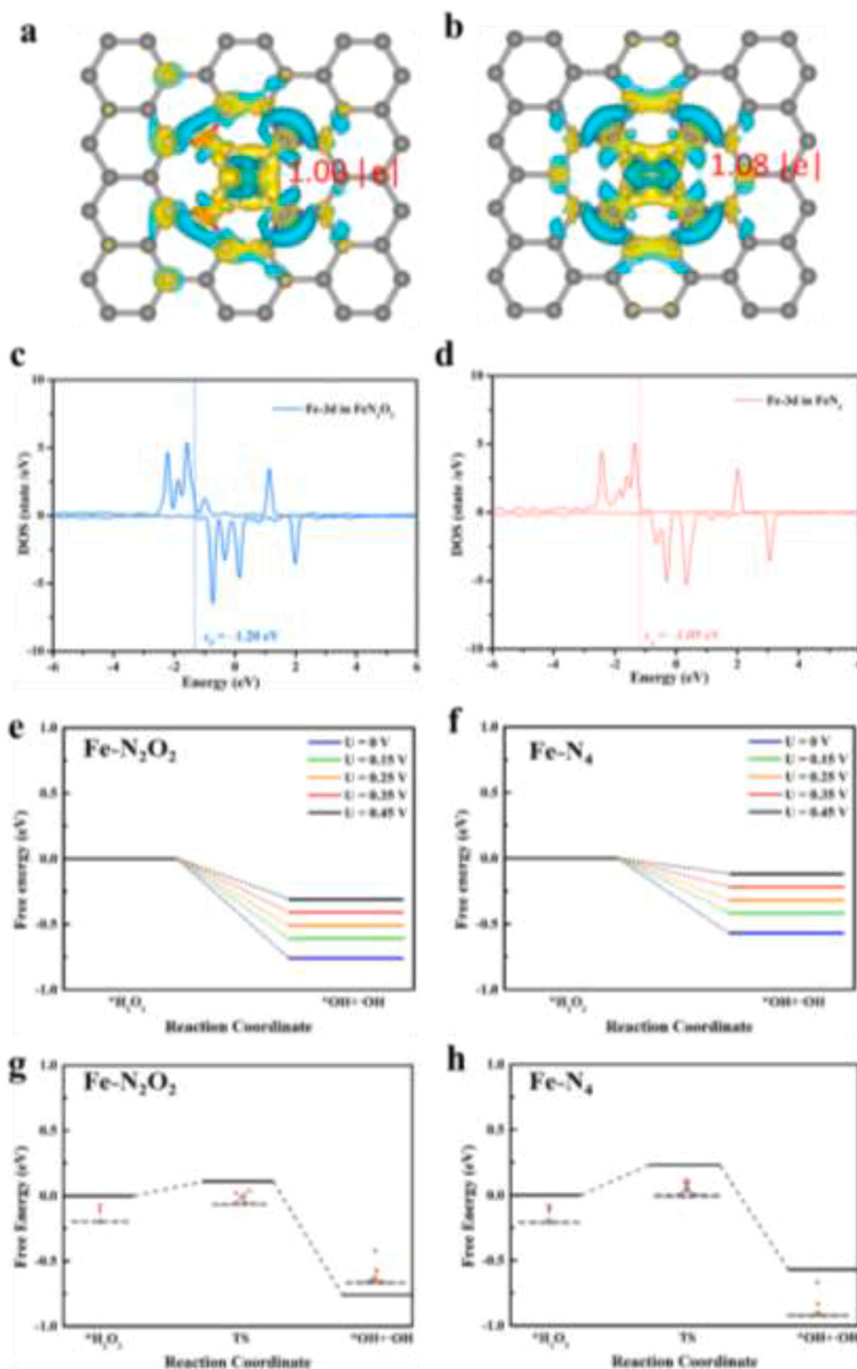
Fig. 4. DFT calculation for differential charge densities (a, b), d-band center value (c, d), free energies at 0/0.15/0.25/0.35/0.45 V vs. RHE (e, f) and reaction kinetic barriers for H_2O_2 reduction to •OH radicals on Fe-N_2O_2 and Fe-N_4 models (g, h).

H_2O_2, subsequently the as-generated H_2O_2 can migrate to the Fe-N_2O_2 site and decomposes into •OH with a lower energy barrier than the Fe-N_4 site. Hence, the highly efficient •OH generation could be achieved on the FeN$_2$O$_2$-HPC that showed a moderate adsorption of H_2O_2 and low energy barrier for H_2O_2 activation to •OH. Consequently, a rational design strategy of a Fe-based SAC for efficient H_2O_2 reduction to •OH is to decrease the adsorption of H_2O_2 of Fe-N_4 catalysts by introducing O atoms, a more negative electronegativity than N, to create relative electron-poor Fe center, thereby slightly promoting the charge state of the iron atom.

3.4. Degradation performance for pollutants

The Hetero-EF performance of the Fe-HPC catalysts for pollutant degradation was evaluated. Phenol was selected as the target pollutant, which is regarded as a kind of typical phenolic compounds and recorded as priority pollutants in the water environment [44]. As depicted in Figure S22a, almost 100 % of phenol was removed in the FeN$_2$O$_2$-HPC Hetero-EF in 90 min, which was higher than that of the FeN$_4$-HPC (59.6 %), and HPC (50.7 %). As illustrated in Figure S23, only 11.1 % and 26.3 % of phenol was removed by the physical adsorption of FeN$_2$O$_2$-HPC and anodic oxidation (AO) process, respectively, indicating the dominant contribution of Hetero-EF in phenol removal. The phenol removal followed the pseudo-first-order kinetics (Figure S22b) and the
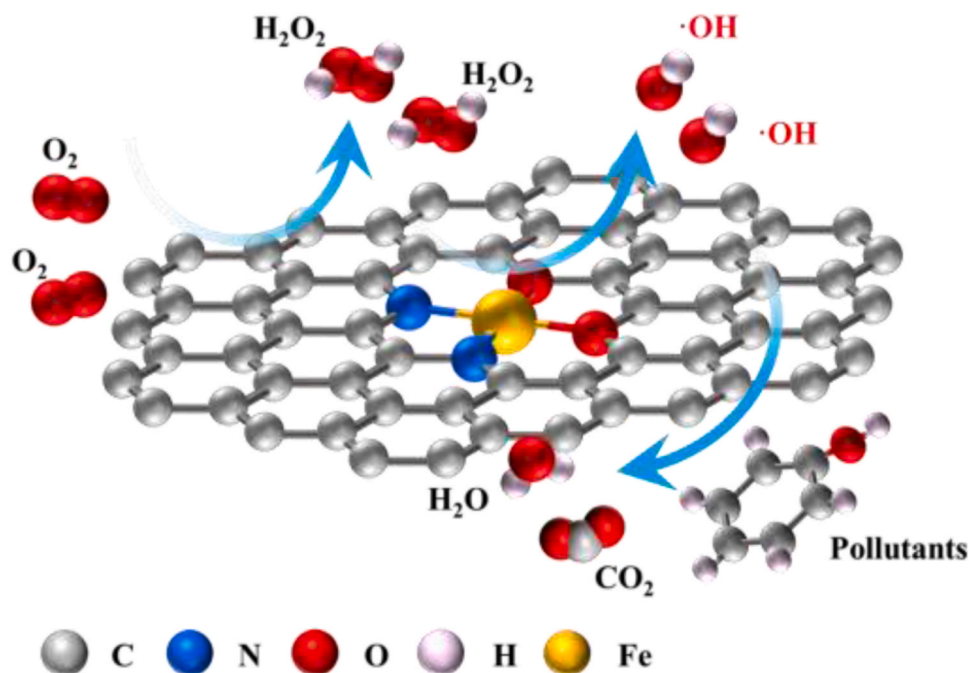
Fig. 5. Proposed catalytic pathways of •OH electrogeneration on FeN_2O_2-HPC. (The yellow, gray, blue, red and pink atoms are Fe, C, N, O, and H atoms, respectively).
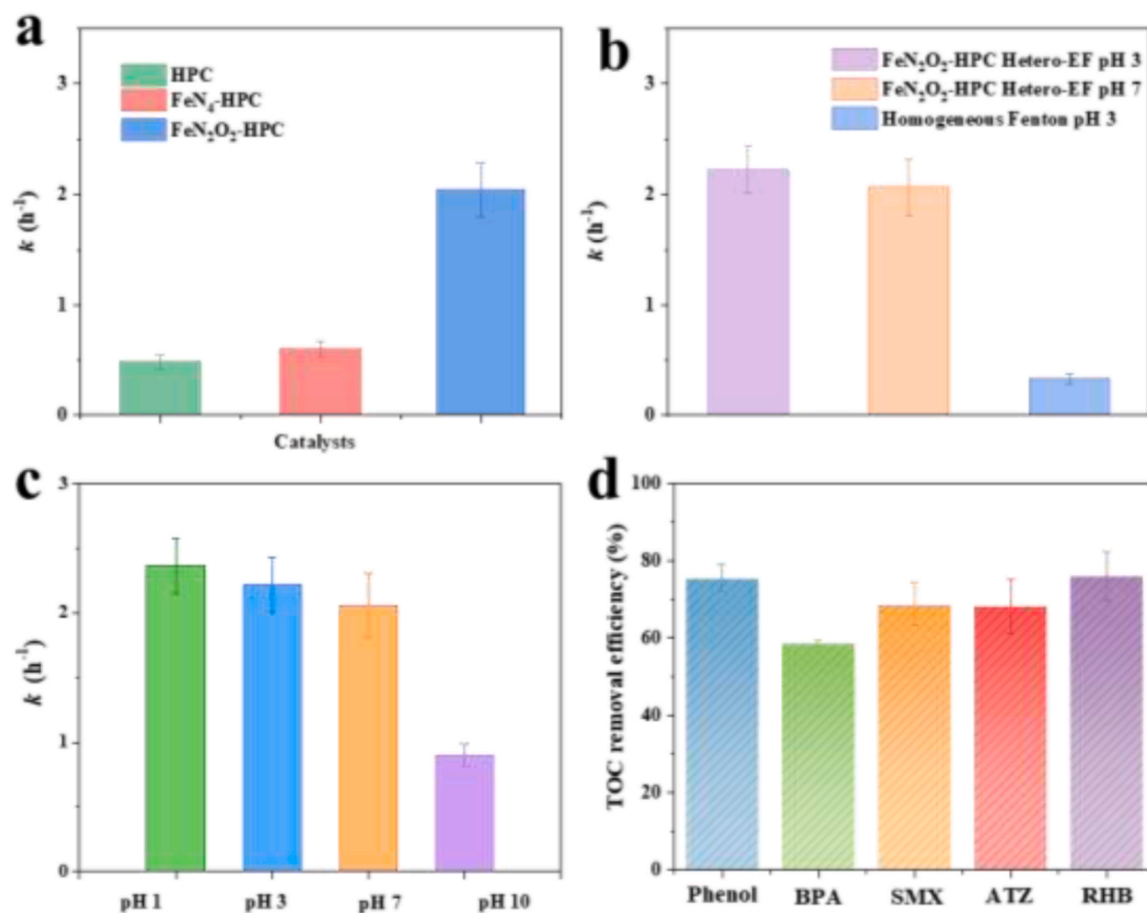

Fig. 6. (a) k of phenol degradation in the Hetero-EF process by FeN_2O_2-HPC, FeN_4-HPC, and HPC cathodes; (b) k of phenol removal by FeN_2O_2-HPC Hetero-EF process at pH 3 and pH 7 and homogeneous Fenton process at pH 3 (c) k of phenol removal at different initial electrolyte pH (1, 3, 7, 10) by the FeN_2O_2-HPC Hetero-EF process; (d) TOC removal of different pollutants (phenol, ATZ, BPA, SMX and RHB) by the FeN_2O_2-HPC Hetero-EF process in 4 h. Reaction conditions: potential $= -0.4$ V vs. SCE, [phenol] $= 20$ mg L^{-1}, [Na_2SO_4] $= 0.05$ mol L^{-1}, O_2 flow rate $=$ Ar flow rate $= 30$ mL min^{-1}.

kinetic rate constant (k) of the catalyst was calculated. FeN_2O_2-HPC displayed sharp increased k of 2.06 h^{-1} for 3.4 ~ 4.3 times higher than that of the FeN_4-HPC (0.60 h^{-1}) and HPC (0.48 h^{-1}) (Fig. 6a). The tendency of phenol removal on the FeN_2O_2-HPC, FeN_4-HPC, and HPC was consistent with the corresponding activity of •OH production. To analyze the reactive oxygen species in phenol degradation, the radical quenching experiments were conducted by TBA and p-benzoquinone (BQ) as •OH and superoxide radical (O_2•$^-$) scavengers. As shown in Figure S24, the phenol removal was hardly influenced after the addition of BQ, indicating the negligible contribution of O_2•$^-$ for phenol degradation. Notably, the phenol degradation rate was decreased to 40 % after adding 700 mmol L^{-1} of TBA, verifying the important role of •OH for phenol degradation of the Hetero-EF process. To further elucidate the role of Fe sites, the Fe-site-shielding experiment was conducted. Generally, electron-rich halide and pseudohalide ions, especially SCN^- species, are employed as guest groups to strongly interact with unsaturated single-atom iron, which can act as Fe-site-shielding agent and alter the local electronic environment [45]. As shown in Figure S25, after adding 1 M KSCN, the phenol removal efficiency dramatically declined from 100 % to 27.5 % in 90 min. This phenomenon demonstrated the key role of FeN_2O_2 single-atom sites for the generation of hydroxyl radicals and the pollutant degradation. Moreover, we compared the performance of the FeN_2O_2-HPC Hetero-EF on pollutant removal with the traditional homogeneous Fenton process. As shown in Figs. 6b and S26, the Hetero-EF of FeN_2O_2-HPC exhibited a kinetic constant of 2.22 h^{-1} at pH 3 and 2.06 h^{-1} at pH 7, which were 6.7 and 6.2 times higher than the Fenton process (0.33 h^{-1} at pH 3) with equal iron loading, highlighting the excellent performance of FeN_2O_2-HPC Hetero-EF system for pollutant degradation. It is well acknowledged that the performance of the Fenton process is dependent on the dosage of Fe^{2+}, and the performance of Fenton process was investigated by multiplying the concentration of Fe^{2+} dosing. As observed in Figure S27, the increasement of Fe^{2+} dosage enhanced the phenol removal rate of the Fenton process, which was slightly higher than FeN_2O_2-HPC Hetero-EF system due to the limited mass transfer of heterogeneous EF process. The FeN_2O_2-HPC Hetero-EF system can obtain efficient phenol removal in the pH range from 1 to 10 (Figs. S28 and 6c), whereas the Fenton process must be operated at pH~3. The performance of phenol removal on the FeN_2O_2-HPC Hetero-EF system at different applied potentials was also explored. As depicted by Figure S29, the $k_{m, cat}$ of phenol removal evidently raised from 0.6 to 6.8 min^{-1} g_{cat}^{-1} with shifting the applied potential from -0.2 to -0.4 V (vs. SCE). However, when the potential further decreased to -0.5 V, the $k_{m, cat}$ declined to 3.2 min^{-1} g_{cat}^{-1}, which could be resulted from the side reaction of hydrogen evolution [46]. Moreover, the degradation and mineralization ability of the FeN_2O_2-HPC Hetero-EF process for different contaminants were investigated. The intermediates of phenol degradation have been identified by GC-MS and Combustion Ion Chromatograph (MCIC). The compound name, chemical structure, formula, molecular weight, and retention time of the phenol degradation intermediates by FeN_2O_2-HPC hetero-EF are listed in Table S9-10. Usually, H_2O_2 and •OH could attack phenol to produce benzenediol (resorcinol, hydroquinone), and degraded by reactive oxygen species (•O_2^-) to form benzoquinone. Subsequently, the benzoquinone undergoes a ring-opening reaction to produce micro-molecular species, such as pentanoic acid, hexanoic acid and so on. Finally, the micro-molecular species were completely oxidized to produce acetic acid and formic acid and eventually mineralized to CO_2 and H_2O [47–50]. Based on the test results and relevant references, the possible pathways of phenol degradation were proposed (Figure S30). Furthermore, the toxicity of phenol and its intermediates were assessed by the Toxicity Evaluation Software Tool (T.E.S.T., developed by the US EPA) for the lethal concentration of Daphnia magna LC_{50}-48 h. According to the Globally Harmonised System of Classification and Labelling of Chemicals (GHS), the toxicity assessment criteria for lethal concentrations of organic pollutants can be categorised as not harmful (>100 mg L^{-1}), harmful (10–100 mg L^{-1}) toxic (1–10 mg L^{-1}) and very

toxic (<1 mg L^{-1}) [51]. As shown in Figure S31, the lethal toxicity of phenol to Daphnia magna decreased gradually during phenol degradation (from 7.4 mg L^{-1} (phenol) to 67.81 mg L^{-1} (hexanoic acid), 154.0 mg L^{-1} (pentanoic acid) and 1036.0 mg L^{-1} (acetic acid)). Therefore, Hetero-EF system treatment was effective in reducing the toxicity of phenol wastewater. The treated wastewater can be safely discharged by prolonging the Hetero-EF system treatment time after complete mineralization of phenol. As displayed in Figure S32, the removal efficiency of phenol, rhodamine B (RHB), bisphenol A (BPA), sulfamethoxazole (SMX) and atrazine (ATZ) reached 96.0 %, 98.5 %, 80.6 %, 77.5 % and 72.0 % within 90 min, respectively. Accordingly, the TOC removal of phenol, RHB, BPA, SMX and ATZ were 75.2 %, 76.0 %, 58.5 %, 68.6 % and 68.2 % in 4 hours, respectively. (Fig. 6d), representing the strong oxidation capability of the FeN_2O_2-HPC Hetero-EF process for mineralization of organic contaminants into CO_2 and H_2O. The stability of the FeN_2O_2-HPC catalysts was assessed by the consecutive cycles for phenol removal. As exhibited in Figure S33, the phenol removal maintained 94.8 % after ten cycles with a slight activity decay of 5.2 % compared with the fresh FeN_2O_2-HPC cathode, manifesting the good stability of FeN_2O_2-HPC catalysts. The corresponding leaching of Fe ions was determined merely to be 0.020 mg L^{-1}, which was only 2 % of total metal content on catalyst.

Furthermore, the treatment of actual industrial wastewater was performed in FeN_2O_2-HPC Hetero-EF process. Coking wastewater is one kind of typical industrial wastewaters including massive refractory and toxic organic pollutants which cannot be treated effectively via conventional wastewater treatment technologies to meet the discharge standards. The actual secondary effluent was obtained from a local coking plant and the initial TOC and COD value were measured to be 66.7 and 247.1 mg L^{-1}, respectively (Table S11). As displayed in Figure S34, the TOC value was reduced from 66.7 to 31.0 mg L^{-1} with the corresponding removal efficiency of 46.5 % after 4 h treatment by the FeN_2O_2-HPC Hetero-EF process. The COD value decreased from 247.1 to 47.3 mg L^{-1}, which met the discharge standard of coking chemical industry (GB 16171–2012, China, 80 mg L^{-1}). The energy consumption of FeN_2O_2-HPC Hetero-EF process was evaluated and the specific energy consumption (SEC) of actual wastewater treatment was calculated to be 23.7 kWh kg_{COD}^{-1} after 4 h treatment, which could be more energy-saving than other electrochemical process previously reported (29.7–68.0 kWh kg_{COD}^{-1}) (Table S12) [52–55].

4. Conclusion

In this work, a FeN_2O_2-HPC single-atom catalyst was designed and synthesized for efficient •OH generation in the Hetero-EF process. DFT calculations demonstrated that the FeN_2O_2 coordination could simultaneously reduce the adsorption energies of *H_2O_2 and energy barrier for efficient •OH generation. The •OH production rate of FeN_2O_2-HPC achieved 25.0 μmol h^{-1}, which exceeded the state-of-the-art electrocatalysts previously reported. Benefited from the high-efficiency production of •OH, the FeN_2O_2-HPC Hetero-EF exhibited excellent activity for organic contaminant removal with a kinetic rate constant of 2.06 h^{-1} for phenol removal at pH 7, exceeding that of the homogeneous Fenton process of 0.33 h^{-1} at pH 3. We prospectively believe that the FeN_2O_2-HPC Hetero-EF can provide a high-efficiency and sustainable method for •OH generation by consuming cheap air, H_2O and electricity, exhibiting attractive advantages for advanced wastewater treatments.

CRediT authorship contribution statement

Hongtao Yu: Methodology, Conceptualization. **Shuo Chen:** Methodology, Conceptualization. **Yan Su:** Software. **Xie Quan:** Writing – review & editing, Supervision, Project administration, Methodology, Conceptualization. **Peike Cao:** Methodology, Investigation, Conceptualization. **Zijun Tan:** Writing – review & editing, Writing – original draft, Methodology, Investigation, Formal analysis, Data curation,

Conceptualization.

Declaration of Competing Interest

The authors declare that they have no known competing financial interests or personal relationships that could have appeared to influence the work reported in this paper.

Data availability

Data will be made available on request.

Appendix A. Supporting information

Supplementary data associated with this article can be found in the online version at doi:10.1016/j.apcatb.2024.124170.

References

[1] J.L. Wang, L.J. Xu, Advanced oxidation processes for wastewater treatment: formation of hydroxyl radical and application, Cri. Rev. Environ. Sci. Technol. 42 (2012) 251–325.

[2] D.B. Miklos, C. Remy, M. Jekel, K.G. Linden, J.E. Drewes, U. Hubner, Evaluation of advanced oxidation processes for water and wastewater treatment - a critical review, Water Res. 139 (2018) 118–131.

[3] P. Neta, R.E. Huie, A.B. Ross, Rate constants for reactions of inorganic radicals in aqueous solution, J. Phys. Chem. Ref. Data 17 (1988) 1027–1284.

[4] P. Wardman, Reduction potentials of one-electron couples involving free radicals in aqueous solution, J. Phys. Chem. Ref. Data 18 (1989) 1637–1755.

[5] Z.-T. Hu, J.-W. Liu, J. Zhao, Y. Ding, Z. Jin, J. Chen, Q. Dai, B. Pan, Z. Chen, J. Chen, Enhanced BiFeO$_3$/Bi$_2$Fe$_4$O$_9$/H$_2$O$_2$ heterogeneous system for sulfamethoxazole decontamination: system optimization and degradation pathways, J. Colloid Inter. Sci. 577 (2020) 54–65.

[6] I. Sires, E. Brillas, M.A. Oturan, M.A. Rodrigo, M. Panizza, Electrochemical advanced oxidation processes: today and tomorrow. a review, Environ. Sci. Pollut. Res. Int. 21 (2014) 8336–8367.

[7] S.O. Ganiyu, M. Zhou, C.A. Martínez-Huitle, Heterogeneous electro-Fenton and photoelectro-Fenton processes: a critical review of fundamental principles and application for water/wastewater treatment, Appl. Catal. B Environ. 235 (2018) 103–129.

[8] K. Liu, J.C. Yu, H. Dong, J.C.S. Wu, M.R. Hoffmann, Degradation and mineralization of carbamazepine using an electro-Fenton reaction catalyzed by magnetite nanoparticles fixed on an electrocatalytic carbon fiber textile cathode, Environ. Sci. Technol. 52 (2018) 12667–12674.

[9] Z. Ai, Z. Gao, L. Zhang, W. He, J.J. Yin, Core–Shell structure dependent reactivity of Fe@Fe$_2$O$_3$ nanowires on aerobic degradation of 4-Chlorophenol, Environ. Sci. Technol. 47 (2013) 5344–5352.

[10] E. Jung, H. Shin, B.-H. Lee, V. Efremov, S. Lee, H.S. Lee, J. Kim, W. Hooch Antink, S. Park, K.-S. Lee, S.-P. Cho, J.S. Yoo, Y.-E. Sung, T. Hyeon, Atomic-level tuning of Co–N–C catalyst for high-performance electrochemical H$_2$O$_2$ production, Nat. Mater. 19 (2020) 436–442.

[11] G.-L. Chai, Z. Hou, T. Ikeda, K. Terakura, Two-Electron oxygen reduction on carbon materials catalysts: mechanisms and active sites, J. Phys. Chem. C 121 (2017) 14524–14533.

[12] H. Zhao, Z.Y. Yuan, Design strategies of non-noble metal-based electrocatalysts for two-electron oxygen reduction to hydrogen peroxide, ChemSusChem 14 (2021) 1616–1633.

[13] Z. Lu, G. Chen, S. Siahrostami, Z. Chen, K. Liu, J. Xie, L. Liao, T. Wu, D. Lin, Y. Liu, T.F. Jaramillo, J.K. Nørskov, Y. Cui, High-efficiency oxygen reduction to hydrogen peroxide catalysed by oxidized carbon materials, Nat. Catal. 1 (2018) 156–162.

[14] Y. Pang, K. Wang, H. Xie, Y. Sun, M.-M. Titirici, G.-L. Chai, Mesoporous carbon hollow spheres as efficient electrocatalysts for oxygen reduction to hydrogen peroxide in neutral electrolytes, ACS Catal. 10 (2020) 7434–7442.

[15] X. Shen, F. Xiao, H. Zhao, Y. Chen, C. Fang, R. Xiao, W. Chu, G. Zhao, In Situ-formed PdFe nanoalloy and carbon defects in cathode for synergic reduction–oxidation of chlorinated pollutants in electro-Fenton process, Environ. Sci. Technol. 54 (2020) 4564–4572.

[16] X. Du, W. Fu, P. Su, L. Su, Q. Zhang, J. Cai, M. Zhou, Trace FeCu@PC derived from MOFs for ultraefficient heterogeneous electro-Fenton process: enhanced electron transfer and bimetallic synergy, ACS EST Eng. 1 (2021) 1311–1322.

[17] Y. Wang, G. Zhao, S. Chai, H. Zhao, Y. Wang, Three-dimensional homogeneous ferrite-carbon aerogel: one pot fabrication and enhanced electro-Fenton reactivity, ACS Appl. Mater. Inter. 5 (2013) 842–852.

[18] S. Weon, D. Huang, K. Rigby, C. Chu, X. Wu, J.-H. Kim, Environmental materials beyond and below the nanoscale: single-atom catalysts, ACS EST Eng. 1 (2020) 157–172.

[19] N. Cheng, L. Zhang, K. Doyle-Davis, X. Sun, Single-atom catalysts: from design to application, Electrochem. Energy Rev. 2 (2019) 539–573.

[20] Q. Zhang, J. Guan, Single-atom catalysts for electrocatalytic applications, Adv. Funct. Mater. 30 (2020) 2000768.

[21] K. Zhao, X. Quan, X. Su, X. Qin, S. Chen, H. Yu, Enhanced chlorinated pollutant degradation by the synergistic effect between dechlorination and hydroxyl radical oxidation on a bimetallic single-atom catalyst, Environ. Sci. Technol. 55 (2021) 14194–14203.

[22] X. Qin, P. Cao, X. Quan, K. Zhao, S. Chen, H. Yu, Y. Su, Highly efficient hydroxyl radicals production boosted by the atomically dispersed Fe and Co Sites for heterogeneous electro-Fenton oxidation, Environ. Sci. Technol. 57 (2023) 2907–2917.

[23] X. Song, H. Zhang, Z. Bian, H. Wang, In situ electrogeneration and activation of H$_2$O$_2$ by atomic Fe catalysts for the efficient removal of chloramphenicol, J. Hazard. Mater. 412 (2021) 125162.

[24] Y. Sun, L. Silvioli, N.R. Sahraie, W. Ju, J. Li, A. Zitolo, S. Li, A. Bagger, L. Arnarson, X. Wang, T. Moeller, D. Bernsmeier, J. Rossmeisl, P. Strasser, Activity–selectivity trends in the electrochemical production of hydrogen peroxide over single-site metal–nitrogen–carbon catalysts, J. Am. Chem. Soc. 141 (2019) 12372–12381.

[25] K. Sun, W. Xu, X. Lin, S. Tian, W.F. Lin, D. Zhou, X. Sun, Electrochemical oxygen reduction to hydrogen peroxide via a two-electron transfer pathway on carbon-based single-atom catalysts, Adv. Mater. Interfaces 8 (2020) 2001360.

[26] Y. Chen, S. Ji, Y. Wang, J. Dong, W. Chen, Z. Li, R. Shen, L. Zheng, Z. Zhuang, D. Wang, Y. Li, Isolated single iron atoms anchored on N-doped porous carbon as an efficient electrocatalyst for the oxygen reduction reaction, Angew. Chem. Int. Ed. 56 (2017) 6937–6941.

[27] Y. Wang, Y. Liu, W. Liu, J. Wu, Q. Li, Q. Feng, Z. Chen, X. Xiong, D. Wang, Y. Lei, Regulating the coordination structure of metal single atoms for efficient electrocatalytic CO$_2$ reduction, Energy Environ. Sci. 13 (2020) 4609–4624.

[28] C.X. Zhao, B.Q. Li, J.N. Liu, Q. Zhang, Intrinsic electrocatalytic activity regulation of M–N–C single-atom catalysts for the oxygen reduction reaction, Angew. Chem. Int. Ed. 60 (2020) 4448–4463.

[29] F. Wang, Y. Zhou, S. Lin, L. Yang, Z. Hu, D. Xie, Axial ligand effect on the stability of Fe–N–C electrocatalysts for acidic oxygen reduction reaction, Nano Energy 78 (2020) 105128.

[30] K. Jiang, S. Back, A.J. Akey, C. Xia, Y. Hu, W. Liang, D. Schaak, E. Stavitski, J. K. Nørskov, S. Siahrostami, H. Wang, Highly selective oxygen reduction to hydrogen peroxide on transition metal single atom coordination, Nat. Commun. 10 (2019) 3997.

[31] Y. Wu, Y. Ding, X. Han, B. Li, Y. Wang, S. Dong, Q. Li, S. Dou, J. Sun, J. Sun, Modulating coordination environment of Fe single atoms for high-efficiency all-pH-tolerated H$_2$O$_2$ electrochemical production, Appl. Catal. B Environ. 315 (2022) 121578.

[32] S.N. Zhao, J.K. Li, R. Wang, J. Cai, S.Q. Zang, Electronically and geometrically modified single-atom Fe sites by adjacent Fe nanoparticles for enhanced oxygen reduction, Adv. Mater. 34 (2021) 2107291.

[33] G. Fang, J. Gao, C. Liu, D.D. Dionysiou, Y. Wang, D. Zhou, Key role of persistent free radicals in hydrogen peroxide activation by biochar: implications to organic contaminant degradation, Environ. Sci. Technol. 48 (2014) 1902–1910.

[34] H. Lin, R. Xiao, R. Xie, L. Yang, C. Tang, R. Wang, J. Chen, S. Lv, Q. Huang, Defect engineering on a Ti$_4$O$_7$ electrode by Ce^{3+} doping for the efficient electrooxidation of perfluorooctanesulfonate, Environ. Sci. Technol. 55 (2021) 2597–2607.

[35] M. Jin, W. Liu, J. Sun, X. Wang, S. Zhang, J. Luo, X. Liu, Highly dispersed Ag clusters for active and stable hydrogen peroxide production, Nano Res. 15 (2022) 5842–5847.

[36] S. Mondal, D. Bagchi, M. Riyaz, S. Sarkar, A.K. Singh, C.P. Vinod, S.C. Peter, In situ mechanistic insights for the oxygen reduction reaction in chemically modulated ordered intermetallic catalyst promoting complete electron transfer, J. Am. Chem. Soc. 144 (2022) 11859–11869.

[37] S. Nayak, I.J. McPherson, K.A. Vincent, Adsorbed intermediates in oxygen reduction on platinum nanoparticles observed by insitu IR spectroscopy, Angew. Chem. Int. Ed. 57 (2018) 12855–12858.

[38] C. Tang, L. Chen, H. Li, L. Li, Y. Jiao, Y. Zheng, H. Xu, K. Davey, S.-Z. Qiao, Tailoring acidic oxygen reduction selectivity on single-atom catalysts via modification of first and second coordination spheres, J. Am. Chem. Soc. 143 (2021) 7819–7827.

[39] K. Wang, D. Huang, W. Wang, Y. Ji, J. Niu, Enhanced perfluorooctanoic acid degradation by electrochemical activation of peroxymonosulfate in aqueous solution, Environ. Int. 137 (2020) 105562.

[40] X. Zhou, D. Xu, Y. Chen, Y. Hu, Enhanced degradation of triclosan in heterogeneous e-Fenton process with MOF-derived hierarchical Mn/Fe@PC modified cathode, Chem. Eng. J. 384 (2020) 123324.

[41] S.-A. Park, H. Lim, Y.-T. Kim, Enhanced oxygen reduction reaction activity due to electronic effects between Ag and Mn$_3$O$_4$ in alkaline media, ACS Catal. 5 (2015) 3995–4002.

[42] H.Y.F. Sim, J.R.T. Chen, C.S.L. Koh, H.K. Lee, X. Han, G.C. Phan-Quang, J.Y. Pang, C.L. Lay, S. Pedireddy, I.Y. Phang, E.K.L. Yeow, X.Y. Ling, ZIF-Induced d-Band modification in a bimetallic nanocatalyst: achieving over 44 % efficiency in the

ambient nitrogen reduction reaction, Angew. Chem. Int. Ed. 59 (2020) 16997–17003.

[43] A.V.R.Ye Xu, Manos Mavrikakis, Adsorption and dissociation of O_2 on Pt-Co and Pt-Fe alloys, J. Am. Chem. Soc. 123 (2004) 4717–4725.

[44] G. Busca, S. Berardinelli, C. Resini, L. Arrighi, Technologies for the removal of phenol from fluid streams: a short review of recent developments, J. Hazard. Mater. 160 (2008) 265–288.

[45] Q. Wang, Z.-Y. Zhou, Y.-J. Lai, Y. You, J.-G. Liu, X.-L. Wu, E. Terefe, C. Chen, L. Song, M. Rauf, N. Tian, S.-G. Sun, Phenylenediamine-based FeNx/C catalyst with high activity for oxygen reduction in acid medium and its active-site probing, J. Am. Chem. Soc. 136 (2014) 10882–10885.

[46] K. Yang, R. Kas, W.A. Smith, T. Burdyny, Role of the carbon-based gas diffusion layer on flooding in a gas diffusion electrode cell for electrochemical CO_2 reduction, ACS Energy Lett. 6 (2020) 33–40.

[47] P. Wang, X. Zhou, J. Wang, J. Miao, R. Zhang, H. Xu, S. Peng, X. Wei, Heterogeneous electro-Fenton system with Co/N-GO modified cathode to degrade phenolic organic pollutants: the main role of singlet oxygen, J. Water Process Eng. 53 (2023) 103850.

[48] T.T.T. Dang, S.T.T. Le, D. Channei, W. Khanitchaidecha, A. Nakaruk, Photodegradation mechanisms of phenol in the photocatalytic process, Res. Chem. Intermediat. 42 (2016) 5961–5974.

[49] I. Othman, J. Hisham Zain, M. Abu Haija, F. Banat, Catalytic activation of peroxymonosulfate using $CeVO_4$ for phenol degradation: an insight into the reaction pathway, Appl. Catal. B Environ. 266 (2020) 118601.

[50] J.A. Zazo, J.A. Casas, A.F. Mohedano, M.A. Gilarranz, J.J. Rodriguez, Chemical pathway and kinetics of phenol oxidation by Fenton's reagent, Environ. Sci. Technol. 39 (2005) 9295–9302.

[51] M. Xu, J. Deng, A. Cai, C. Ye, X. Ma, Q. Li, S. Zhou, X. Li, Synergistic effects of UVC and oxidants (PS vs. Chlorine) on carbamazepine attenuation: mechanism, pathways, DBPs yield and toxicity assessment, Chem. Eng. J. 413 (2021) 127533.

[52] X. Liu, X. Yu, L. Sha, Y. Wang, Z. Zhou, S. Zhang, The preparation of black titanium oxide nanoarray via coking fluorinated wastewater and application on coking wastewater treatment, Chemosphere 270 (2021) 128609.

[53] X. Zhu, J. Ni, P. Lai, Advanced treatment of biologically pretreated coking wastewater by electrochemical oxidation using boron-doped diamond electrodes, Water Res. 43 (2009) 4347–4355.

[54] C.R. Wang, Z.F. Hou, M.R. Zhang, J. Qi, J. Wang, Electrochemical oxidation using BDD anodes combined with biological aerated filter for biotreated coking wastewater treatment, J. Chem. 2015 (2015) 1–7.

[55] K. Zhao, X. Quan, S. Chen, H. Yu, J. Zhao, Preparation of fluorinated activated carbon for electro-Fenton treatment of organic pollutants in coking wastewater: the influences of oxygen-containing groups, Sep. Purif. Technol. 224 (2019) 534–542.